

SOOT FORMATION IN LAMINAR DIFFUSION FLAMES

M. D. Smooke, M. B. Long and B. C. Connelly
Department of Mechanical Engineering
Yale University
New Haven, CT

and

M. B. Colket and R. J. Hall
United Technologies Research Center
East Hartford, CT

Abstract

Laminar, sooting, coflow diffusion flames at atmospheric pressure have been studied experimentally and theoretically as a function of fuel dilution by inert nitrogen. The flames have been investigated with laser diagnostics. Laser extinction has been used to calibrate the experimental soot volume fractions and an improved gating method has been implemented in the laser-induced incandescence (LII) measurements resulting in differences to the soot distributions reported previously. Numerical simulations have been based on a fully-coupled solution of the flow conservation equations, gas-phase species conservation equations with complex chemistry, and the dynamical equations for soot spheroid growth. The model also includes the effects of radiation re-absorption through an iterative procedure. An investigation of the computed rates of particle inception, surface growth and oxidation, along with a residence time analysis, helps explain the shift in the peak soot volume fraction from the centerline to the wings of the flame as the fuel fraction increases. The shift arises from changes in the relative importance of inception and surface growth combined with a significant increase in the residence time within the annular soot formation field leading to higher soot volume fractions, as the fuel fraction increases.

*Corresponding Author: Mitchell D. Smooke
Department of Mechanical Engineering
Yale University
P.O. Box 208284
New Haven, CT 06520-8284
(203) 432-4344 (Work)
(203) 432-6775 (FAX)
mitchell.smooke@yale.edu

SOOT FORMATION IN LAMINAR DIFFUSION FLAMES

Introduction

Hydrocarbon growth processes in flames are important both to the understanding of soot production from combustion systems and for the development of continuous processes for the manufacture of carbon-based materials. In addition to direct health effects of combustion-generated soot and polyaromatic hydrocarbons, the temperature decrease due to radiative losses can affect flame length and other temperature-dependent processes such as the formation of NO_x . Similarly, in flames in which substantial fractions of fuel carbon are converted to soot, the temporary removal of gas-phase carbon can shift the local $\text{H}_2/\text{H}_2\text{O}$ and CO/CO_2 conversion ratios and affect the local temperatures.

Practical combustion devices include gas turbines, furnaces, and internal combustion engines. While premixed or partially premixed flames may be appropriate for selected applications, the vast majority of large-scale industrial combustion applications utilize non-premixed flames. As the local equivalence ratio in a non-premixed (diffusion flame) varies, the propensity to form soot changes. After the fuel is (oxidatively) pyrolyzed in fuel-rich zones, soot precursors form, and given sufficient residence time, these will nucleate and grow into soot particles. In practical devices operating within design conditions, soot should oxidize nearly to completion prior to the burner exit.

Unfortunately, temporary changes in operating conditions (as well as turbulent fluctuations) can momentarily cause the equivalence ratio in the oxidative part of the flame to be reduced dramatically. Such conditions can allow soot particles to pass through the flame unconsumed. The results of unoxidized soot can vary from the coating of furnace walls in a commercial boiler (having an adverse effect on the heat transfer characteristics in the system), to the impingement of soot particles on the turbine blades of an engine. The results can affect $\text{PM}_{2.5}$ emissions [1] as well as contrail visibility and IR signature issues. Even if all of the soot formed in the diffusion flame were oxidized to

CO, temporarily localized equivalence ratio reductions might inhibit complete oxidation to CO₂, resulting in, for example, high (gaseous) exhaust emissions [2]. Thus, the study of sooting flames remains important from practical, economic, environmental and safety standpoints, as well as for purely scientific interests in the fundamental processes.

Previously, we described and utilized a detailed soot growth model in which the dynamical equations for particle production were coupled to the flow and gaseous species conservation equations. Results from the model were compared to experimental data for a confined methane-air flame and a series of unconfined ethylene-air flames [3,4,5]. The configuration for these flames (see Fig. 1) includes a central jet of gaseous fuel diluted with nitrogen, surrounded by a co-annular stream of air. Both probe (thermocouple and gas-sampling techniques) and optical diagnostic methods (Rayleigh scattering and laser-induced incandescence) were used to measure the temperature, gas species and soot volume fractions. The two-dimensional system couples detailed transport and finite rate chemistry in the gas phase with the aerosol dynamical equations in the sectional representation. The formulation includes models for the treatment of inception, surface growth, oxidation, and coalescence of soot particulates. Effects of thermal radiation and particle scrubbing of gas phase growth and oxidation species were also included.

In the more recent of these studies [4,5], we investigated the changing soot field as the dilution fuel fraction in the central tube changed (32%, 40%, 60%, and 80% ethylene). We were able to predict soot volume fractions along the wings of the flame in good agreement with experimental measurements; but we under predicted soot volume fractions along the centerline. This deficiency was particularly true for the flames with higher fuel mole fractions. The transition from peak soot along the centerline to peak soot along the wings (observed both in our experiments and in our modeling) is qualitatively consistent with the early work of Santoro and coworkers [e.g., 6,7], although in the prior work, the fuel jet was undiluted and the transition in the soot field was observed by increasing the fuel jet velocity.

It is the objective of this present work to refine both the prior computations (to include self-absorption and refined gridding) and the experimental measurements of the soot distributions, to extend our simulations to other flames, and to interrogate the computational solutions. In particular, this latter objective is performed to develop a clearer understanding of the causes for the transition of the peak soot volume fraction from the centerline to the wings of the flame as the fuel fraction increases. Specifically, in this paper, we continue our investigation of soot formation in diffusion flames by investigating the relationship of the inception, surface growth and oxidation submodels together with particle residence times within the flame. While varying the diluent level is an established method of varying soot production in diffusion flames [7,8], there have been limited studies of the centerline to wing shift in soot profiles that occur with dilution. Experimentally, the LII measurements have been repeated using a detector with improved temporal response and an on-line extinction technique has been added to calibrate the soot volume fraction measurements.

In the following section, we review the details of the soot model. The experimental methods and the computational methodology are contained in the subsequent two sections. The results and interpretations from the solutions complete the paper.

Soot Formation Model

The soot formation model is described in detail in [5]. For completeness, we outline only the essential features:

Inception

The model is based on the sequence of growing naphthalenyl to pyrenyl through sequential acetylene addition, H-atom elimination, H-atom abstraction, and acetylene addition followed by ring closure. Overall, the reaction can be written $C_{10}H_7 + 3C_2H_2 \Leftrightarrow C_{16}H_9 + 2H + H_2$. This sequence is assumed to continue to form yet larger PAH structures with the overall balance of $C_{10}H_7 + 3nC_2H_2 \Leftrightarrow C_{10+2n}H_{7+2n} + 2nH + nH_2$.

Quasi steady-state concentrations of intermediate polycyclic aromatic hydrocarbons are assumed, leading to steady-state expressions for the formation rates of these high molecular weight condensed polycyclic aromatic hydrocarbons (PAH). The computed soot results are relatively independent of the number, n , assigned to the inception species and equal to 21 in this work. Limitations and major assumptions of the model are discussed in more detail in [3,4]. Scrubbing of gas phase species by soot growth processes, generally accounted for, was neglected for inception because the kinetic models utilized in this study already under predict benzene mole fractions by approximately a factor of two (see also, [3]). The inception rate was not augmented by the factor of two included in [5]. This results in predicted soot volume fractions lower than in [5] but more consistent with the new experimental measurements reported below.

Surface Growth and Oxidation

The surface growth model used in the numerical simulations was based on the premixed flame data of Harris-Weiner [9] where we assumed an activation energy of $E_s = 31.8$ kcal/mole [10] and where we multiplied the nominal Arrhenius factor by two (see also [3-5]). Surface growth is first order in acetylene concentration in this model. (Also available is the ‘MODFW’ surface growth mechanism [11], as corrected by [12] and referred to as the ‘CH’ model. This ‘CH’ model was shown to be successful in modeling soot growth in high temperature flames [13] and is similar to the HACA model [14]). Oxidation of soot by O_2 and OH is treated as described in [3,4]. In the assumed free-molecule regime, surface growth and oxidation rates are proportional to particle surface area.

Particle Dynamics

The growth of soot particles is modeled as a free-molecule aerosol dynamics problem, using the well-known sectional particle size representation for spheres [15]. The application of this approach to soot modeling is described in [3-5,16]. The contributions from the inception processes are incorporated as a source term in the dynamical equation

for the first sectional bin, whose lower mass boundary is set equal to the mass of the assumed inception species. Calculated results were not significantly sensitive to the number of sections assumed, with 20 sections used in all the calculations reported here.

The spherical particle sectional model nominally imposes no constraint on the final particle size, and does not account for aggregate formation. Coalescence destroys particle surface area, whereas aggregation, to the first order, does not. This is an important consideration because of the dependence of surface growth and oxidation on particle surface area. Adding equations for the number of primary spheroids within a section would make it possible to model accurately the formation of soot aggregates [17,18,19], but this is beyond the scope of the present paper. Instead, an approximate treatment of aggregate formation effects on surface area has been employed, as will be discussed.

Radiative Power Loss

For flames with sub-ppm soot volume fractions, the power radiated from soot and gas bands (CO₂, H₂O, and CO, using the exponential wideband model) is computed in the optically thin limit using the expressions in [20]. These flames will lose a very significant fraction of flame enthalpy due to radiation, and temperatures can be significantly depressed, affecting both flame chemistry and soot formation. In higher soot loading flames, the optically thin model tends to overestimate the radiation losses. In principle, some re-absorption of thermal emissions can occur, particularly on or near the centerline, which receives emissions from surrounding regions of the flame. This optical thickness effect reduces the net rate of thermal radiation energy loss and locally raises the temperature. More complex calculations of the local net emission rate including re-absorption were undertaken using the “discrete transfer” method of Lockwood and Shah [21] and the narrowband RADCAL algorithm [22]. The computational procedure was discussed in [5], where re-absorption was found to produce soot centerline-to-wing ratios in better agreement with experiment. While temperature changes associated with radiation re-absorption are not large, the great sensitivity of soot growth to temperatures makes incorporation of these effects important.

Soot Ageing

Two principal deficiencies of the soot model used in [3,4] were that (i) centerline soot was always substantially under predicted and (ii) the computed wings of the flame were extended much beyond those determined by experiment. The original model allowed the formation of primary particles that were much larger than typical maximum experimental values (~25nm). These large particles slowed the oxidation process and caused the extended sooting region. In practice, soot primary particles reach a maximum size due to active surface site deactivation (ageing). Dobbins [23] has given a measured deactivation rate for the process, and some modeling of the effect has been carried out in premixed flames [19,24]. Hall and Colket [19] used a decay rate similar to that of Dobbins in a study of aggregate formation using sectional analysis, and Singh, et. al. [24] tested different functional dependences of surface reactivity on age in their study of high pressure coagulation using Monte Carlo techniques. Frenklach and co-workers [25,26] have fitted to various premixed flame data an empirical expression for the fraction of active sites that is a function of the average particle size and gas temperature, but not explicitly to individual particle age. Much remains uncertain about how to model this effect, particularly in a diffusion flame, however. Given this uncertainty, in this work a simple step function dependence of surface reactivity on particle size was assumed in which growth is shut off above a cut-off particle size (25 nm in these simulations).

Further, to simulate approximately the preservation of particle surface area in aggregate-aggregate collisions, coalescence was disallowed above a certain particle size, denoting a boundary between “liquid” particles and larger aggregates. Particles of this size (again 25 nm was chosen) and larger will not coalesce with each other. Coalescence is still allowed for all collisions involving “liquid” particles, and hence particles larger than 25 nm can still be formed in the simulations by small particle scrubbing. Particles with sizes larger than 25 nm can be crudely viewed as aggregated particles with multiple individual spheroids. This is an approximate treatment of particle morphology that we plan ultimately to improve by adding equations for the number of primary spheroids within

each aggregate size class. The primary particle size at which coalescence ceases and particles start to fuse together to form aggregates might ultimately be more accurately determined from a multi-component sectional analysis in which the de-hydrogenation of the particles is calculated. Such a multi-component analysis might also be a route to calculating ageing effects more accurately. Even with the heuristic modifications to surface growth and coalescence, as adopted here, primary particle size was limited and the extended soot wings were eliminated, consistent with the experimental data.

Experimental Approach

The details of the burner and diagnostic approaches are similar to those described in [3]. Atmospheric pressure, axisymmetric, coflowing, nonpremixed laminar flames were generated with a burner in which the fuel flows from an uncooled 4.0 mm inner diameter vertical brass tube (wall thickness 0.38 mm) into a concentric, 50 mm diameter air coflow. The fuel was a mixture containing varying ratios of ethylene and nitrogen. The fuel and oxidizer flows are set with an average cold-flow velocity of 35 cm/sec. Electronic mass flow controllers, with long-term accuracy to within 5%, governed the flow rates. The same burner apparatus was used for all experiments.

Experimental data quantifying the soot volume fraction of the flames were obtained using two-dimensional laser-induced incandescence (LII) measurements [27-30] calibrated with an on-line extinction method [31]. Both the LII excitation and the extinction calibration used a frequency-doubled Nd:YAG laser (532 nm), with the beam focused into a sheet across the centerline of the burner. A laser fluence of approximately 0.3 J/cm^2 was used for the LII measurements since, in this range, the detected signal was independent of small variations in the laser sheet profile and beam extinction across the flame did not result in a loss of signal. The LII signal was captured using a fast-gate (10-ns response time) intensified CCD camera. A gate time of 23 ns was used, with the intensifier fully on upon arrival of the laser pulse. A broadband filter centered at 405 nm with a bandwidth of 70 nm was placed in front of the camera. The raw LII images were averaged and corrected for luminosity and optical throughput. These images were further corrected for a left-right nonuniformity characteristic of the fast-gate intensifier and the

10-mm data slices were then combined to generate composite soot volume fraction images covering the entire flame.

Previous experiments [3] used an intensifier gate time of 1 μs , due to slow intensifier response times. Such long gate times, however, tend to over-count the larger particles with respect to the smaller ones because larger particles take longer to cool to flame temperatures after the initial laser heating. This effect can cause problems with both the soot volume fraction distribution as well as with the calibration procedure. The lower concentration flames tend to have smaller particles, which are undercounted if a long gate time is used. As an illustration of the need for short gate times, Fig. 2 displays the ratio of the peak LII intensities for the 80% and 32% flames as the gate time is varied from 5 - 1000 ns. The ratio decreases steadily as the gate time is reduced from 1000 ns, and levels off for gate times below 50 ns. It can be seen that an error of more than a factor of two would result in the soot volume fraction of 32% flame relative to the 80% flame if the longer gate times were used for the LII detection.

The extinction calibration was carried out at a laser fluence of less than 0.01 J/cm^2 , low enough to avoid unwanted LII effects and altering the properties of the soot. The laser beam was separated by a beam splitter into an extinction beam, which follows the same path through the flame as the LII beam, and a reference beam, which does not traverse the flame. After it is partially extinguished by the flame, the extinction beam is re-collimated, and the extinction and reference beams are then aligned so that they travel parallel to one another, but at different heights. The two beams are focused into sheets by a cylindrical lens, and are incident on a dye cell containing a mixture of Rhodamine 640 and ethanol. The fluorescence of the dye cell is imaged by a CCD camera through a long-pass filter at 570 nm, which filters out light scattered from the incident laser. The relative intensities of the extinction and reference beams are used to determine how much of the laser is extinguished by the flame. The average soot volume fraction across the flame diameter is then determined using the Lambert-Beer law in the Rayleigh approximation [29], and the result is used to calibrate the LII images. Here, the dimensionless soot extinction coefficient is taken to be 10 [32,33], which is the same value used for the

numerical calculations. The on-line extinction calibration was performed only on the higher concentration flames (80% and 60% ethylene), and the results were extrapolated to the lower concentration flames (40% and 32% ethylene), since uncertainties in the calibration of the lower concentration flames began to dominate when the total extinction dropped below a few percent.

Computational Approach

The axisymmetric computational model [3,4] employs the gas-phase diffusion flame equations in the velocity-vorticity formulation with buoyancy and the particle sectional approach presented in [16]. The result is a strongly coupled set of elliptic partial differential equations. The gas and soot equations are additionally coupled through non-adiabatic radiative loss. Radial and axial velocities, the vorticity, the temperature, the gas-phase species and the particle sectional mass fractions are computed. The chemical mechanism was derived from one of the more comprehensive and well-validated sets available for ethylene [34] (see also [5,35,36]). The resultant mechanism contains 476 reactions and 66 chemical species. Twenty soot sections are included in the formulation. The result is a model that requires a total of 90 dependent variables to be solved at each grid point. The system is closed with the ideal gas law and appropriate boundary conditions are applied on each side of the computational domain. Local properties are evaluated via transport and chemistry libraries. The sectional thermophoretic velocities in the free molecule regime are given in [16] as are the sectional diffusion velocities written with a mass-weighted mean diffusion coefficient for each size class. The governing conservation equations are solved on a two-dimensional mesh by combining a Newton-based steady-state and a time-dependent solution method [5]. A time-dependent solution is first obtained on a coarse grid and then grid points are inserted adaptively to increase the resolution in regions of high spatial activity. Computations were performed on an AMD Dual Opteron 240 system running at 1.4 GHz.

Discussion of Results and Interpretations

In Figure 3 we plot the soot volume fraction contours as the fuel fraction in the central tube changes from 32% to 80%. The corresponding experimental (LII) measurements of the soot volume fractions are illustrated in Figure 4 (note that both the computational and experimental soot volume fraction plots have their own color scale). Both the computational and the experimental results indicate that, as the fuel mole fraction increases, the location of the peak soot transitions from the tip of the flame along the centerline to the wings of the flame. This movement of the location of the peak soot is qualitatively consistent with the early work of Santoro and coworkers [e.g., 6,7], although in their work the fuel jet was undiluted and the transition in the soot field was observed by increasing the fuel jet velocity. In our results, as the fuel mole fraction increases, the percentage ratio of the peak soot along the centerline to the overall peak soot decreases from 100% in the 32% flame to approximately 50% in the 80% flame. The peak soot volume fractions for the experimental and numerical results are illustrated in Figure 5 as a function of the fuel mole fraction. Also shown are the peak soot centerline comparisons. Figures 3, 4 and 5 demonstrate that the model is able to reproduce both the peak soot volume fractions as well as the relative soot distributions for the flames studied in this paper.

To understand the centerline to wing transition more fully, the relative contributions of the three submodel processes contributing to soot formation—inception, surface growth and oxidation have been examined. As discussed earlier, the inception model utilizes steady-state expressions for the formation of a high molecular weight condensed polycyclic aromatic hydrocarbon (PAH), and the surface growth rate is first order in acetylene concentration. Soot oxidation by both OH and molecular oxygen is included but the reaction with OH usually dominates due to its high super equilibrium levels in the flame front [4]. The oxidation rate with soot is based upon the work of Neoh, et al. [37]

In Figs. 6-9, contours for each of these processes in the four different flames are illustrated. For both the 32% (Fig. 6) and 40% (Fig. 7) flames, several features are visible immediately. The maximum inception and surface growth rates occur along the centerline near the tip of the flame and the maximum inception rate increases from the 32% to the 40% flame. Above the soot tip, oxidation increases and soot is removed from the flames. The highest oxidation rates are along the centerline of the flames, directly downstream of the high soot concentrations. The high inception rates and commensurate high surface growth rates near the peak of the flames are the direct cause of the peak soot concentrations along the centerline for these flames.

We note the unusual halo occurring in the surface growth contours in Figs. 6-9. This halo is caused by a cessation of surface growth (indicative of the separation in the blue zone) as the peak particle diameter exceeds the maximum diameter allowed for surface growth (25 nm), as described in the section on soot ageing. Oxidation then produces some particles below 25 nm at which point surface growth can resume. The halo is an artifact of our treatment of soot ageing that allows for late stage surface growth. Its overall contribution to total soot formation is small.

The location of the peak soot volume fraction is noticeably shifted in the higher fuel flames (Figs. 3-4 and Figs. 8-9). In the 60% and 80% flames, the peak inception rate still occurs along the centerline near the tip of the flame. However, these values are about a factor of two lower than the corresponding peak surface growth rates that occur fairly low in the flame along the wings. Also, the surface growth rates along the sides of these flames are larger relative to those along the centerline. As a result, the peak soot volume fractions in these flames occur along the wings. In addition, as the ratio of the peak inception rate along the centerline to the peak surface growth rate along the wings decreases, the corresponding ratio of soot volume fraction also decreases. Soot oxidation increases further downstream and is largest in the upper portions of the wings where the highest soot levels occur.

The results of the submodel investigation are useful in illustrating why the soot occurs in one region versus another. However, they do not elucidate the reasons as to why the inception rates are always highest on the centerline for the lower fuel fraction flames and why the maximum values of soot inception along the centerline differ by only 50% in all four cases. In addition, they do not explain why the surface growth rates become larger along the wings as the fuel mole fraction increases and why these values increase by nearly a factor of two and a half. Based on many studies of soot formation in laminar, premixed flames (e.g., [9,12,38]), and expectations from the soot dynamical equations, we know that residence time in the flame plays an important role in the formation of soot and soot precursors. In Fig. 10 we plot, for each of the flames, the soot volume fraction along the centerline of the flame as a function of the fluid dynamic residence time (defined as the integral in the axial direction of the reciprocal of the axial velocity). We note that for all four flames the soot begins to increase after 15-20 milliseconds. For the 32% and 40% flames, the transit time through the sooting cone is about 10-15 milliseconds while in the 60% and 80% flames this value increases from 25 to nearly 40 milliseconds.

From Fig. 10, the time available for inception and surface growth along the centerline (prior to the peak value and subsequent oxidation) increases from about 3 to 7 to 14 to 20 milliseconds as the dilution level decreases, respectively, for the four flames studied. Hence, there is more than a factor of six increase in the available time for inception and growth; yet, the increase in the soot volume fraction is less than a factor of three. (In a coalescence-dominated regime with no oxidation in which total soot surface area is relatively constant, soot volume fraction might be expected to increase linearly with residence time [11]. For a regime with weak coalescence and no oxidation, simple analysis shows that soot particle mass/volume fraction might be expected to vary as the cube of the residence time). For the 80% flame, a significant reduction in the soot formation rates is apparent. This non-linear relationship is reminiscent of the well-established saturation of the soot volume fraction observed in premixed (burner-stabilized) flames. (e.g., [38,39]). This phenomenon is partially simulated through the soot ageing feature associated with our model. In Fig. 10, however, it is apparent that not

only is the maximum soot volume fraction decreased substantially below a linear relationship (with time), but also the formation slope is substantially decreased for the higher fuel loading. The most important cause for this significant decrease in soot production rates is the decrease in flame temperatures along the flame centerline, due to increased radiative losses in the less diluted flames. (Computed radiative power loss varies from 13%-26% as the fuel fraction increases.) As shown in Figs. 11 and 12, the peak temperatures in the soot-forming region decrease from about 1800 to 1600K between the 32% and 80% flames, respectively. As described by Glassman [40], temperature is one of the more important parameters in describing the soot formation field, and the assumed 31.8 kcal/mole activation energy gives the surface growth rate used in this study a strong temperature dependence. The net result is that, even with the significant increase in residence time along the centerline (and the local increase in fuel fraction) associated with the less diluted flames, the ageing of the soot particles and the lower temperatures inhibit the enhanced soot inception and growth along the centerline.

Normalization of both the soot and the height (using $\eta = z\mathcal{D}/\dot{V}$, where z is the axial height, \mathcal{D} is the species diffusivity $\sim 0.136 \text{ cm}^2/\text{sec}$, and \dot{V} is the volumetric flow rate) results in the curves shown in Fig 12. This normalization function for the height has been used by Santoro, et al. [6] and Kent and Wagner [41] for comparing experimental flames with different flow rates. The qualitative trends observed here are nearly identical to those presented previously although the value of η at which the peak soot is observed is ~ 0.065 in the present work vs. ~ 0.18 in [6]. This factor of nearly 2.8 is attributable to the difference in diameters of the central fuel tubes used in the two studies (0.4 cm vs. 1.1 cm). The relatively early formation of the soot is associated with the higher fuel fractions in these flames.

Centerline temperatures are also reproduced in Fig. 12. The earlier rise in the temperatures with increasing ethylene levels as a function of η is due to the increased fuel flowing through the central tube. The premature decay in centerline temperatures for the 80% flame occurs due to significant radiation loss at elevated soot levels for this flame; the temperature partially recovers as the stoichiometric surface arrives, leading to

additional heat release. The position of the second peak is nearly coincident with the position of the peaks in the 32% and 40% flames.

In all four flames, the surface growth begins to increase along the wings several millimeters above the inlet and reaches a maximum value less than one centimeter downstream. In the 32% and 40% flames, this region lies between 1.0-1.5 centimeters from the conical region of the flame tip. The region of soot growth increases to nearly 4.0 cm in the 80% flame. Hence, as was the case in the centerline analysis, there is additional time for surface growth (and inception) to generate more soot along the wings.

A clearer picture of the residence times along the wings of the flames is illustrated in Figure 13. In these pictures we have plotted constant time lines at 5 millisecond intervals on the soot volume fraction contours. The positions of the constant time contours are nearly identical for the four different flames. While perhaps surprising, this similarity is a direct result of the identical flow velocities (35 cm/sec) for both the gas in the fuel tube and the surrounding coflowing air stream. By comparing the results in Fig. 13 with those in Figs. 6-9, we observe that the surface growth along the wings peaks between 10-15 milliseconds. Furthermore, the computed time lines clearly show that the particles leading up to the top of the wings of the 60% and 80% flames reside just inside the flame front for an additional 20 and 25 milliseconds, respectively, compared to approximately 10-15 milliseconds for the 32% and 40% flames.

The much higher concentration of soot along the sides of these flames (relative to that along the centerline) for the 60% and 80% flames creates a collision-dominated coalescence zone that contributes to the rapid formation of relatively larger soot particles and agglomerated structure as the tip of the wings are approached. After 20 milliseconds within the low fuel fraction flames, oxidation begins to destroy soot in the wings so that any additional growth in the wings is reduced dramatically. In the higher fuel fraction flames, however, soot growth along the wings can continue for at least another 20-25 milliseconds before the effects of oxidation are felt. The particles in the higher fuel fraction flames have low surface to volume ratios and longer lifetimes in the downstream

oxidation zones. Hence, soot particulates are emitted preferentially from these regions, typically when flame temperatures have decreased (principally via radiative cooling) below 1500K. Moreover, while both the centerline and the wings have increased residence time, Fig. 14 illustrates that the wings retain the higher temperatures in the higher fuel fraction flames, leading to more soot growth.

In particular, the color scale in Fig. 14 has been adjusted to highlight temperature differences among the flames. The increased temperatures with increased fuel fraction in the central tube contribute significantly to the high soot production region leading up to the wings of the flames. As a result, in comparison to the centerline region where decreases in temperature counterbalance the increased residence time, in the annular regions inside the flame front, both the increased residence time and increased temperatures contribute to much higher levels of soot production.

The shorter residence time in the lower fuel fraction flames is a direct result of the combination of the lower fuel content of the central jet and the diffusion of oxygen causing the stoichiometric surface to close earlier downstream compared to the higher fuel fraction flames. Presumably, if the residence time for the higher fuel fraction flames can be reduced or the residence time for the lower fuel fraction flames can be increased, the balance of wing to centerline soot can be changed. To explore this hypothesis, we have reduced the fuel and coflow inlet velocities of the 80% flame by a factor of two. Computational and experimental soot volume fraction contours along with inception, surface growth and oxidation contours are illustrated in Figs. 15, 16, and 17, respectively. The flame is reduced in height dramatically due to the smaller volumetric fuel flow rate and the location of the soot and its peak value are in good agreement between the computation and the experiment. Of particular note is the spatial location of the three subprocesses compared to the higher velocity case in Fig. 9. The peak surface growth in the wings is reduced by approximately 25%, the inception peaks on the centerline and it is a factor of two larger than in the higher velocity flame. The combination of these results causes a major change in the distribution of the soot in the flame.

Conclusions

Laminar, sooting, coflow diffusion flames have been studied experimentally and computationally as a function of ethylene fuel dilution. Soot profiles obtained from laser-induced soot incandescence undergo a shift away from the flame centerline toward the wings of the flame as the ethylene fraction and sooting levels increase. Theoretical simulations agree well with these results. Model predictions have been improved by approximate treatments of particle ageing and aggregate formation, as well as by a precise treatment of radiative re-absorption effects. The large impact of radiative power loss on temperature has a significant effect on soot formation.

Investigation of the relative rates of inception, surface growth, and oxidation, along with a particle residence time analysis, are shown to explain the shift of soot away from the centerline as the fuel fraction increases. While inception tends to peak on the centerline, the maximum in surface growth migrates from the centerline to the wings of the flame as the fuel fraction increases. Concurrently, the relative importance of surface growth and inception reverses. This change in the relative importance of these two subprocesses is due to the significant increase in residence time available for soot growth in the flame wings. By altering the inlet velocities of the higher fuel fraction flame, we are able to modify the available residence time along the wings so as to generate soot profiles similar to those of a lower fuel fraction flame. The level of soot on the centerline increases with respect to that on the wings as the peak centerline to wing temperature also increases.

Acknowledgements

In 1988, two of the authors (MDS and MLB) met with Bob Bilger to talk about using optical imaging techniques and computational modeling to obtain a better understanding of the structure of coflow laminar diffusion flames. Most of the combined computational and experimental studies of laminar flames to that date were focused on one-dimensional systems. While imaging methods had been developed a few years earlier, they had yet to

be used quantitatively in comparisons with computations. Bob stressed that, if an experimental and modeling study were to be performed on a multidimensional flame, it should take place in a simple configuration that minimized effects of the burner and the laboratory environment. The result was the unconfined, lifted, coflow configuration that has been used in over a dozen of our studies since those days in the late 1980's. Bob has had a major influence on our research program and we are extremely appreciative to him for his insight, guidance and suggestions.

The authors (MDS and MBL) would also like to acknowledge support for this work from the DOE Office of Basic Energy Sciences (Dr. Frank Tully, contract monitor), the National Science Foundation (Dr. Linda Blevins, contract monitor) and NASA (Dr. Karen Weiland, contract monitor) under contracts DE-FG02-88ER13966, CTS-0328296, and NNC04AA03A, respectively. In addition, one of the authors (MBC) gratefully acknowledges the Strategic Environmental Research and Development Program (SERDP) under a contract coordinated by Dr. Mel Roquemore of the Air Force Research Laboratories (Wright Patterson AFB). We are also grateful to Mr. Brian Dobbins for his assistance in the preparation of the figures.

References

1. U.S. Environmental Protection Agency, National Ambient Air Quality Standards for Particulate Matter: Final Decision, Federal Registrar, 62 FR 38652, July 18, 1997
2. Puri, R., Santoro, R. J., and Smyth, K. C., *Comb. Flame*, **97**, 125-144 (1994).
3. McEnally, C., Shaffer, A., Long, M. B., Pfefferle, L., Smooke, M. D., Colket, M. B., and Hall, R. J., *Proceedings of the Combustion Institute*, **27**, 1497-1505 (1998).
4. Smooke, M. D., McEnally, C. S., Pfefferle, L. D., Hall, R. J., and Colket, M. B., *Comb. Flame*, **117**, 117-139 (1999).
5. Smooke, M. D., Hall, R. J., Colket, M. B., Fielding, J., Long, M. B., McEnally, C. S., and Pfefferle, L. D., *Comb. Theory and Modelling*, **8**, 593-606 (2004).
6. Santoro, R. J., Semerjian, H. G., and Dobbins, R. A., *Comb. Flame*, **51**, 203-218 (1983).
7. Santoro, R. J. and Semerjian, H. G., *Proceedings of the Combustion Institute*, **20**, 997-1006 (1984).
8. Santoro, R. J., Yeh, T. T., Horvath, J. J., and Semerjian, H. G., *Combust. Sci. and Tech.*, **53**, 89-115 (1987).
9. Harris, S.J., and Weiner, A.M., *Combust. Sci. Tech.*, **31**, 155-167 (1983).
10. Hura, H.S. and Glassman, I., *Proceedings of the Combustion Institute*, **22**, 371-378 (1988).
11. Colket, M.B., and Hall, R.J., in *Soot Formation in Combustion, Mechanisms and*

- Models*, H. Bockhorn, Ed., Springer Series in Chemical Physics, **59**, Springer-Verlag, p. 442, (1994).
12. Xu, F., Sunderland, P. B., Faeth, G. M., *Combust. Flame*, **108**, 471-493 (1997).
 13. Smooke, M.D., Yetter, R.A., Parr, T.P., Hanson-Parr, D.M., Tanoff, M.A., Colket, M.B., and Hall, R.J., *Proceedings of the Combustion Institute*, **28**, 2013-2020 (2000).
 14. Frenklach, M., and Wang, H., *Proceedings of the Combustion Institute*, **23**, 1559-1566 (1990).
 15. Gelbard, F., and Seinfeld, J.H., *J. Coll. Int. Sci.*, **78**, 485-501 (1980).
 16. Hall, R.J., Smooke, M.D., and Colket, M.B., in *Physical and Chemical Aspects of Combustion: A Tribute to Irvin Glassman*, ed. by R.F. Sawyer and F.L. Dryer, Combustion Science and Technology Book Series, Gordon and Breach, (1997).
 17. Rogak, S.N., PhD Dissertation, Cal. Tech., (1991).
 18. Rogak, S.N., *Aerosol Sci. Tech.*, **26**, 127-140 (1997).
 19. Hall, R. J. and Colket, M. B. "Calculations of Soot Aggregate Growth and Oxidation Using a Sectional Size Representation", Paper #79, Fall Technical Meeting of the Eastern States Section of the Combustion Institute, Raleigh, North Carolina, pp. 348-350, October 13-15 (1999).
 20. Hall, R.J., *J. Quant. Spectrosc. Radiat. Transfer*, **51**, 635-644 (1994).
 21. Lockwood F.C. and Shah, N.G., *Proceedings of the Combustion Institute*, **18**, 1405-1414 (1981).

22. Grosshandler, W.L., *RADCAL: A Narrow-Band Model for Radiation Calculations in a Combustion Environment*, NIST Technical Note 1402 (1993).
23. Dobbins, R. A., *Comb. Science and Tech*, **121**, 103 (1996).
24. Singh, J., Balthasar, M., Kraft, M., Wagner, W., *Proceedings of the Combustion Institute*, **30**, 1457-1466 (2005).
25. Kazakov, A., Wang, H., Frenklach, M., *Combust. Flame*, **100**, 111–120 (1995).
26. Appel, J., Bockhorn, H., Frenklach, M., *Combust. Flame*, **121**, 122–136 (2000).
27. Quay, B., Lee, T.-W., Ni, T., and Santoro, R. J., *Combust. Flame*, **97**, 384-392 (1994).
28. Vander Wal, R.L., and Weiland, K.J., *Applied Physics B*, **59**, 445-452 (1994).
29. Zhao, H., and Ladommatos, N., *Progress in Energy and Combustion Science*, **24**, 221-225 (1998).
30. Mewes, B., and Seitzman, J.M., *Applied Optics*, **36**, 709-717 (1997).
31. Axelsson, B., Collin, R., and Bengtsson, P.E., *Applied Physics B*, **72**, 367-372 (2001).
32. Krishnan, S.S., Lin, K.C., and Faeth, G.M., *Journal of Heat Transfer*, **123**, 332-339 (2001).
33. Williams, T.C., Shaddix, C.R., Jensen, K.A., and Suo-Anttila, J.M., “Measurement of the Dimensionless Extinction Coefficient of Soot within Laminar Diffusion Flames,” *Proceedings of the Joint Meeting of the U.S. Sections of the Combustion Institute*, Philadelphia, PA (2005).

34. Sun, C. J., Sung, C. J., Wang, H., and Law, C.K., *Combust. Flame*, **107**, 321-335 (1996). A copy of the modified mechanism is available on request (colketmb@utrc.utc.com)
35. Liu, F., Guo, H., Smallwood, G. J., and Gulder, O. L., *Comb. Theory and Modelling*, **7**, 301-316 (2003).
36. Guo, H., Liu, F., and Smallwood, G. J., *Comb. Theory and Modelling*, **8**, 475-490 (2004).
37. Neoh, K.G., Howard, J.B., and Sarofim, A.F., "Soot Oxidation in Flames" in *Particulate Carbon: Formation During Combustion*, ed. by D.C. Siegla and G.W. Smith, p. 261, Plenum Press, New York, 1981.
38. Haynes, B. S. and Wagner, H. Gg., *Z. Phys. Chem. N.F.*, **133**, 201-213 (1982).
39. Bockhorn, H. and Schafer, T., "Growth of Soot Particles in Premixed Flames by Surface Reactions", in *Soot Formation in Combustion, Mechanisms and Models*, H. Bockhorn, Ed., Springer Series in Chemical Physics, **59**, Springer-Verlag, p. 253, (1994).
40. Glassman, I., *Proceedings of the Combustion Institute*, **22**, 295-311 (1989).
41. Kent, J.H. and Wagner, H. Gg., *Combust. Sci. and Tech.*, **41**, 245-269 (1984).

Figure Captions

Figure 1. Schematic of the coflow diffusion flame.

Figure 2. The ratio of the peak LII signals from the 80% and 32% ethylene flames as a function of intensifier gate time.

Figure 3. Computational soot volume fractions as a function of the fuel fraction.

Figure 4. Measurements (LII) of soot volume fractions as a function of the fuel fraction.

Figure 5. Experimental and numerical peak soot volume fractions and peak centerline soot volume fractions as a function of the fuel mole fraction.

Figure 6. Computed contours of inception, surface growth and (-) oxidation rates (gm/cc/sec) for the 32% ethylene flame.

Figure 7. Computed contours of inception, surface growth and (-) oxidation rates (gm/cc/sec) for the 40% ethylene flame.

Figure 8. Computed contours of inception, surface growth and (-) oxidation rates (gm/cc/sec) for the 60% ethylene flame.

Figure 9. Computed contours of inception, surface growth and (-) oxidation rates (gm/cc/sec) for the 80% ethylene flame.

Figure 10. Centerline soot volume fractions as a function of residence time.

Figure 11. Centerline temperatures as a function of residence time.

Figure 12. Normalized soot volume fraction and centerline temperatures as a function of the normalized height.

Figure 13. Contours of soot volume fractions along with isopleths of residence times.

Figure 14. Temperature isotherms with isopleths of residence times. Note the adjustment of the color scale to illustrate the higher wing temperatures as the fuel fraction increases.

Figure 15. Computational soot volume fraction for the lower velocity 80% flame.

Figure 16. Experimental (LII) soot volume fraction for the lower velocity 80% flame.

Figure 17. Computed contours of inception, surface growth and (-) oxidation rates (gm/cc/sec) for the lower velocity 80% flame.

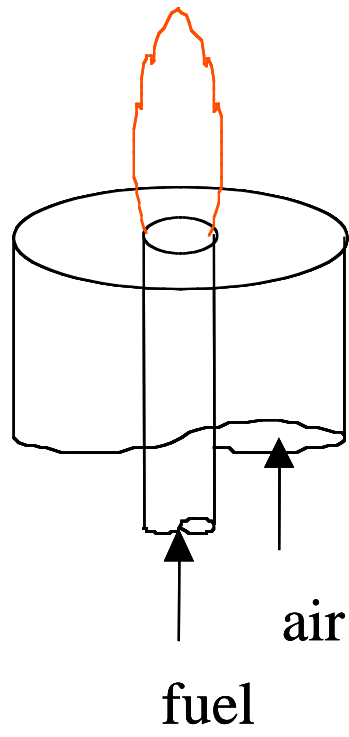


Figure 1. Schematic of the coflow diffusion flame.

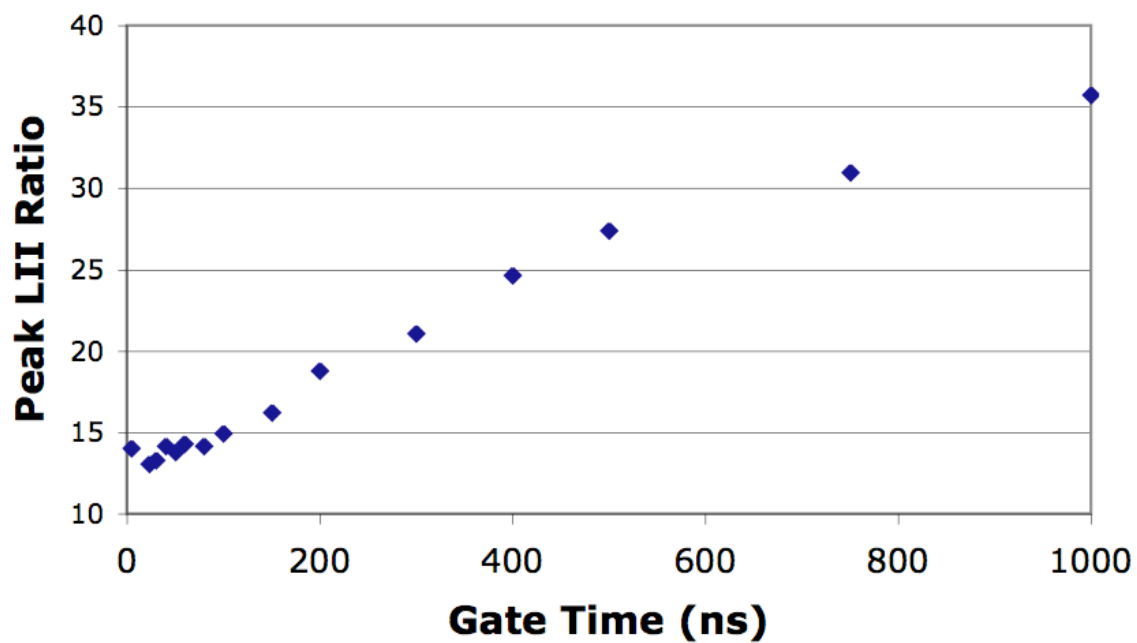


Figure 2. The ratio of the peak LII signals from the 80% and 32% ethylene flames as a function of intensifier gate time.

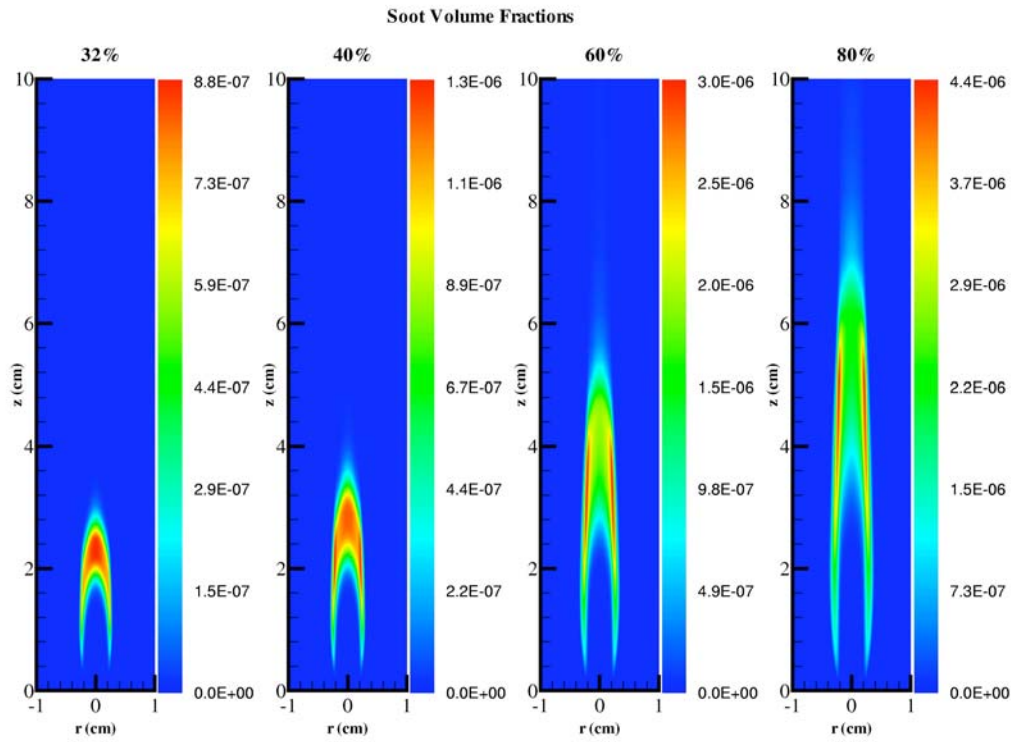


Figure 3. Computational soot volume fractions as a function of the fuel fraction.

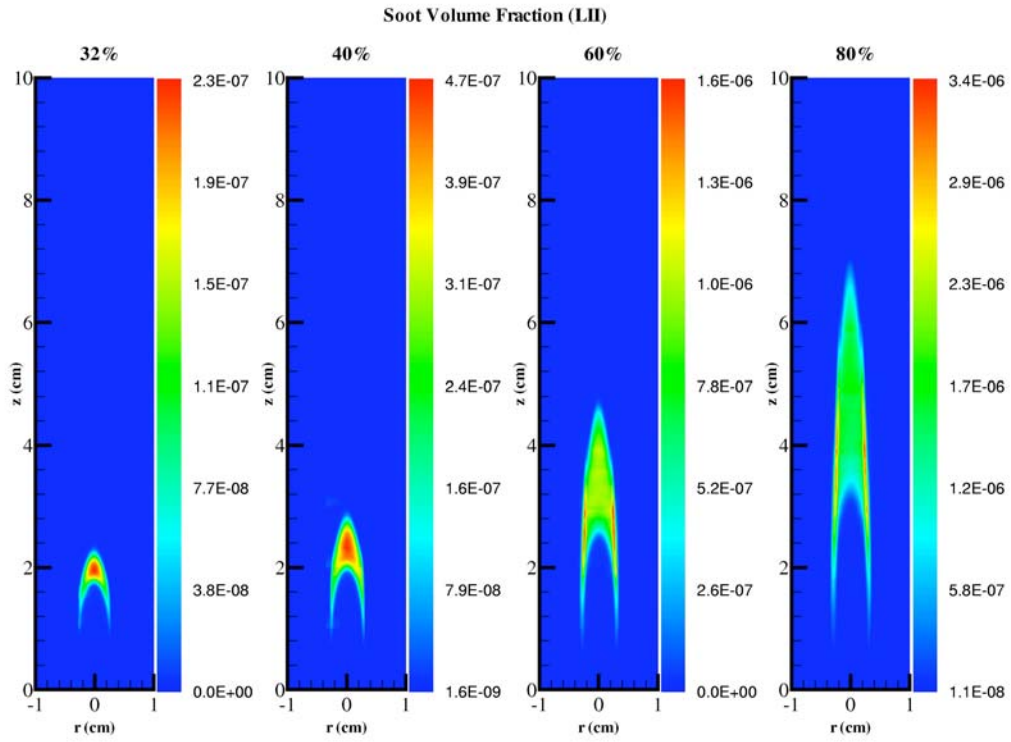


Figure 4. Measurements (LII) of soot volume fractions as a function of the fuel fraction.

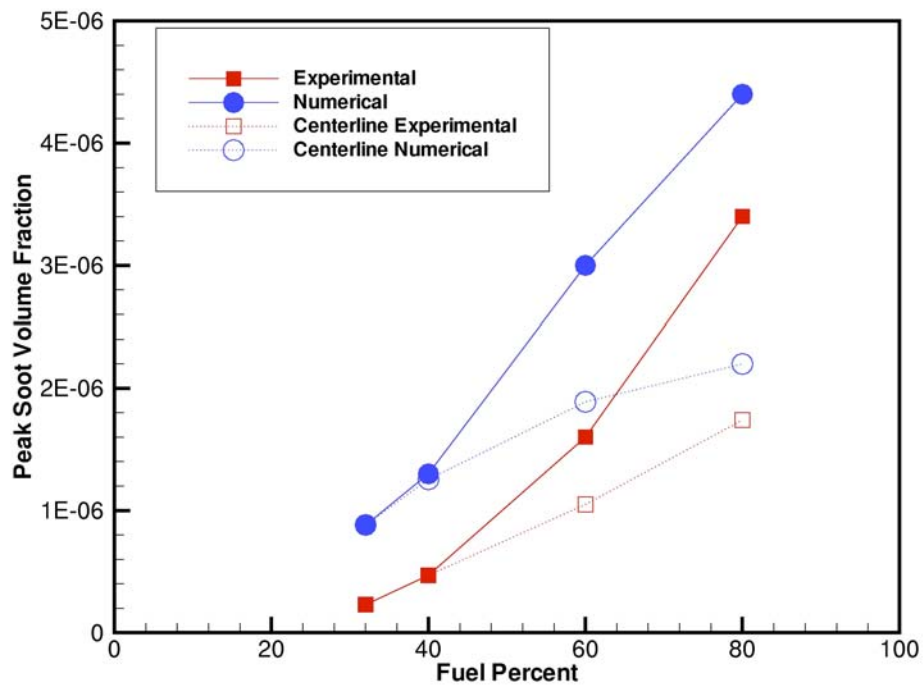


Figure 5. Experimental and numerical peak soot volume fractions (solid symbols) and peak centerline soot volume fractions (open symbols) as a function of the fuel mole fraction.

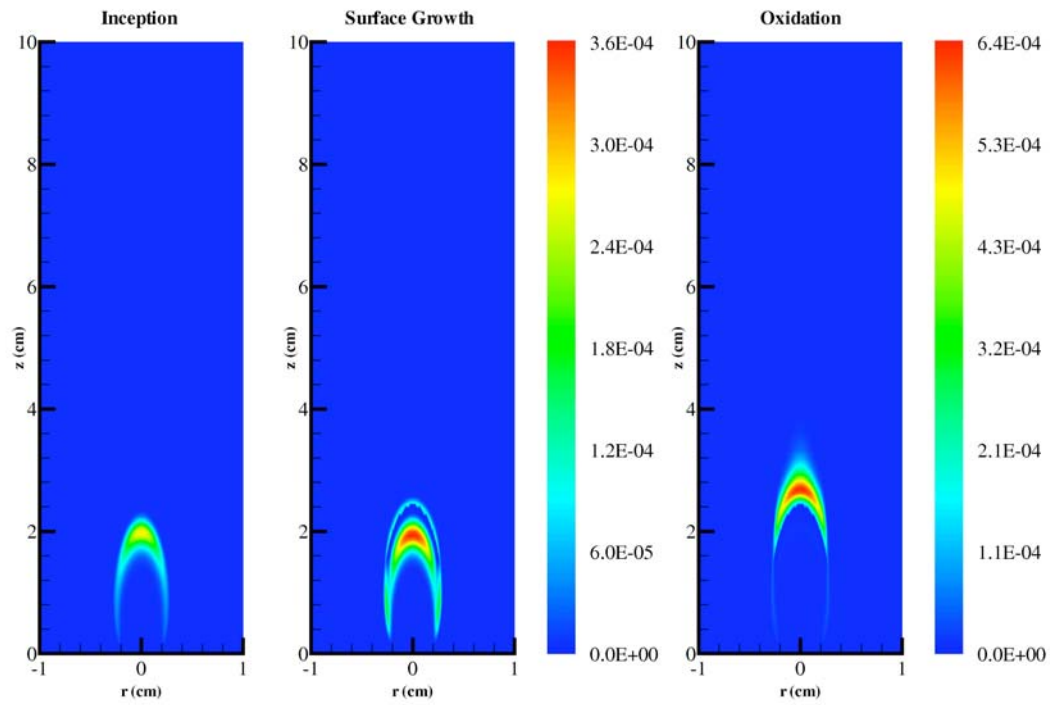


Figure 6. Computed contours of inception, surface growth and (-) oxidation rates (gm/cc/sec) for the 32% ethylene flame.

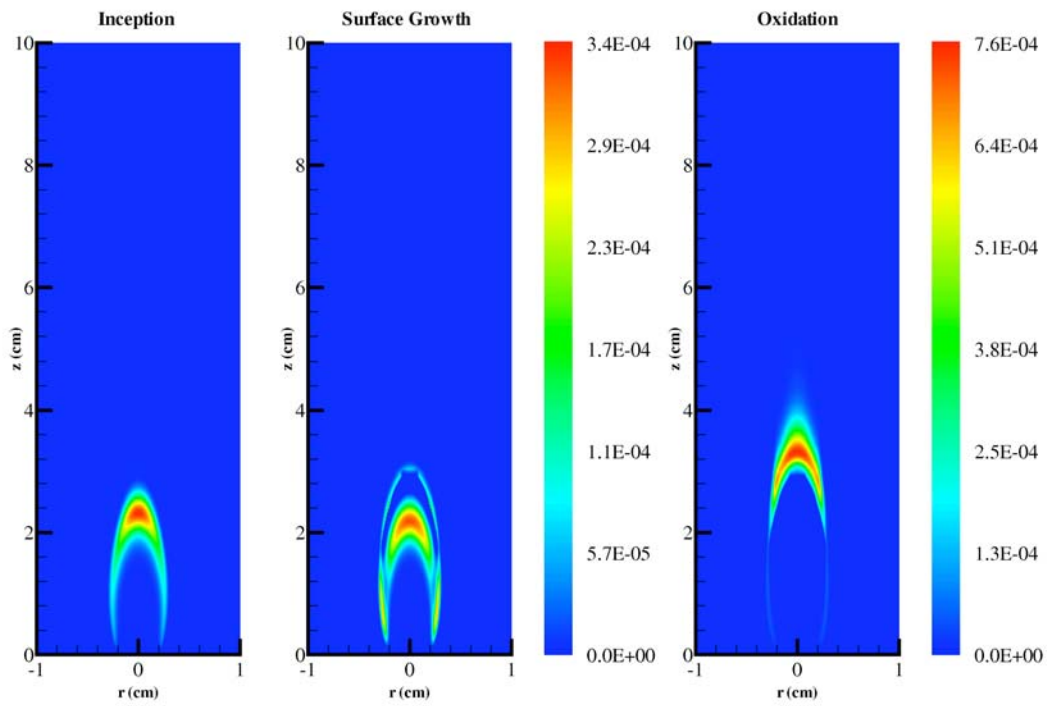


Figure 7. Computed contours of inception, surface growth and (-) oxidation rates (gm/cc/sec) for the 40% ethylene flame.

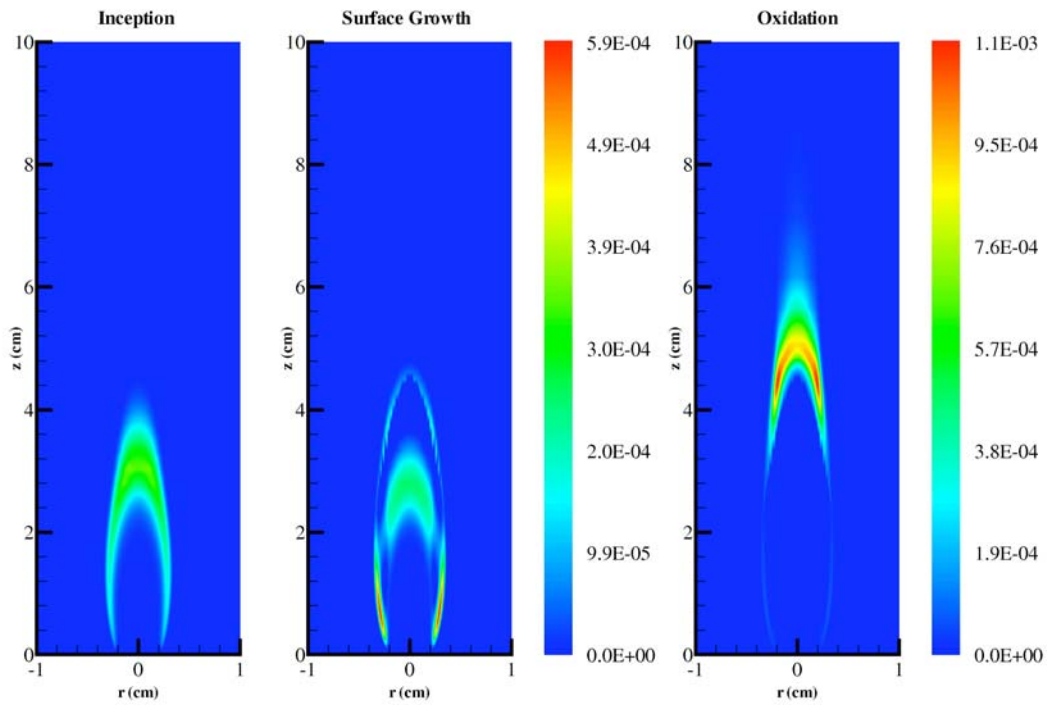


Figure 8. Computed contours of inception, surface growth and (-) oxidation rates (gm/cc/sec) for the 60% ethylene flame.

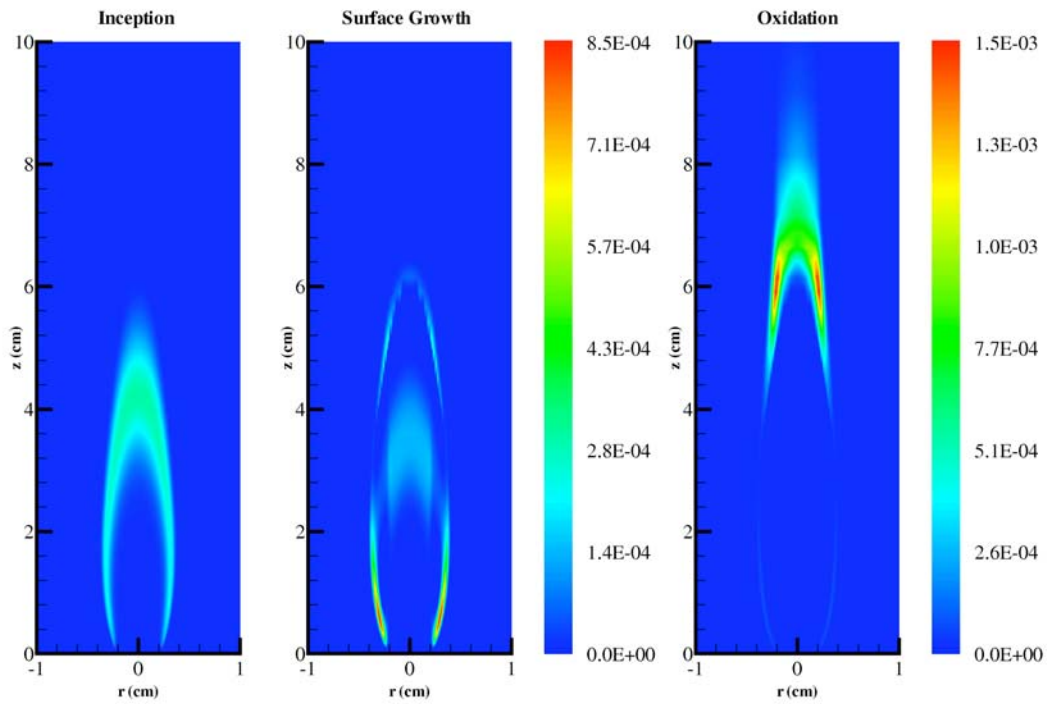


Figure 9. Computed contours of inception, surface growth and (-) oxidation rates (gm/cc/sec) for the 80% ethylene flame.

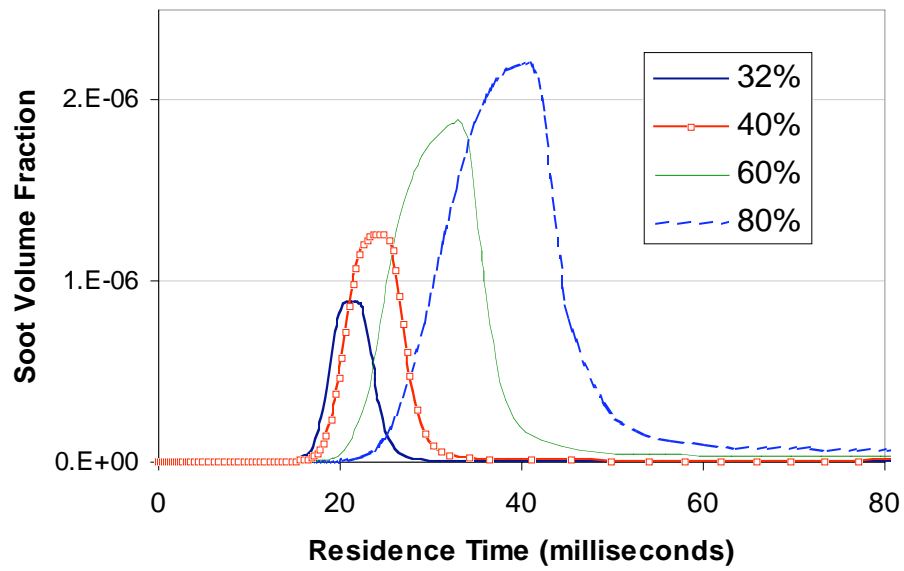


Figure 10. Centerline soot volume fractions as a function of residence time.

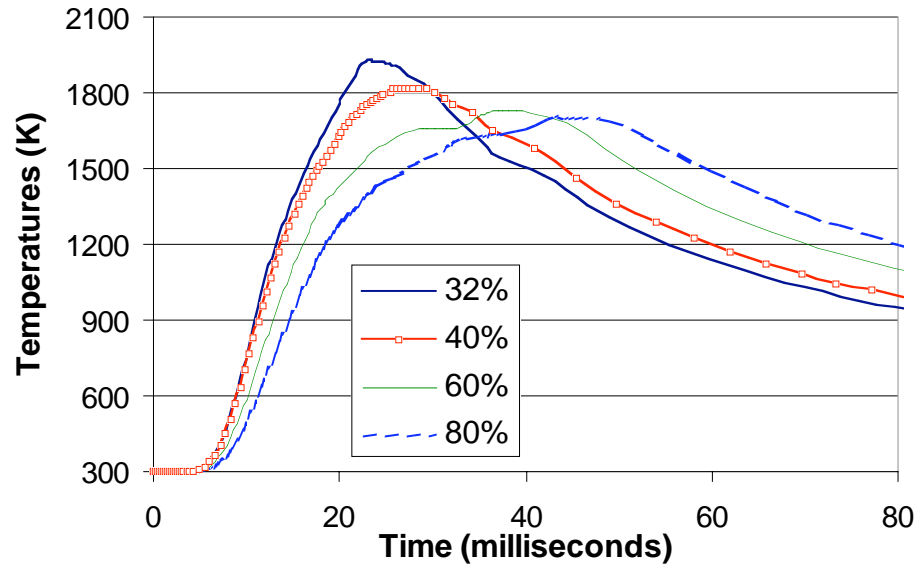


Figure 11. Centerline temperatures as a function of residence time.

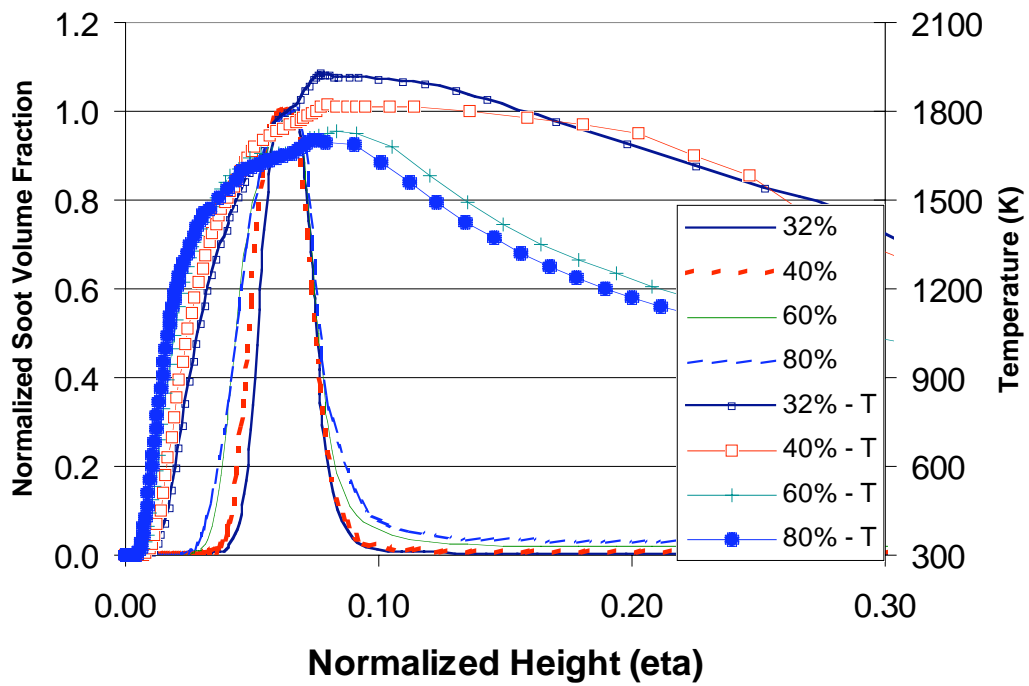


Figure 12. Normalized soot volume fraction and centerline temperatures as a function of the normalized height.

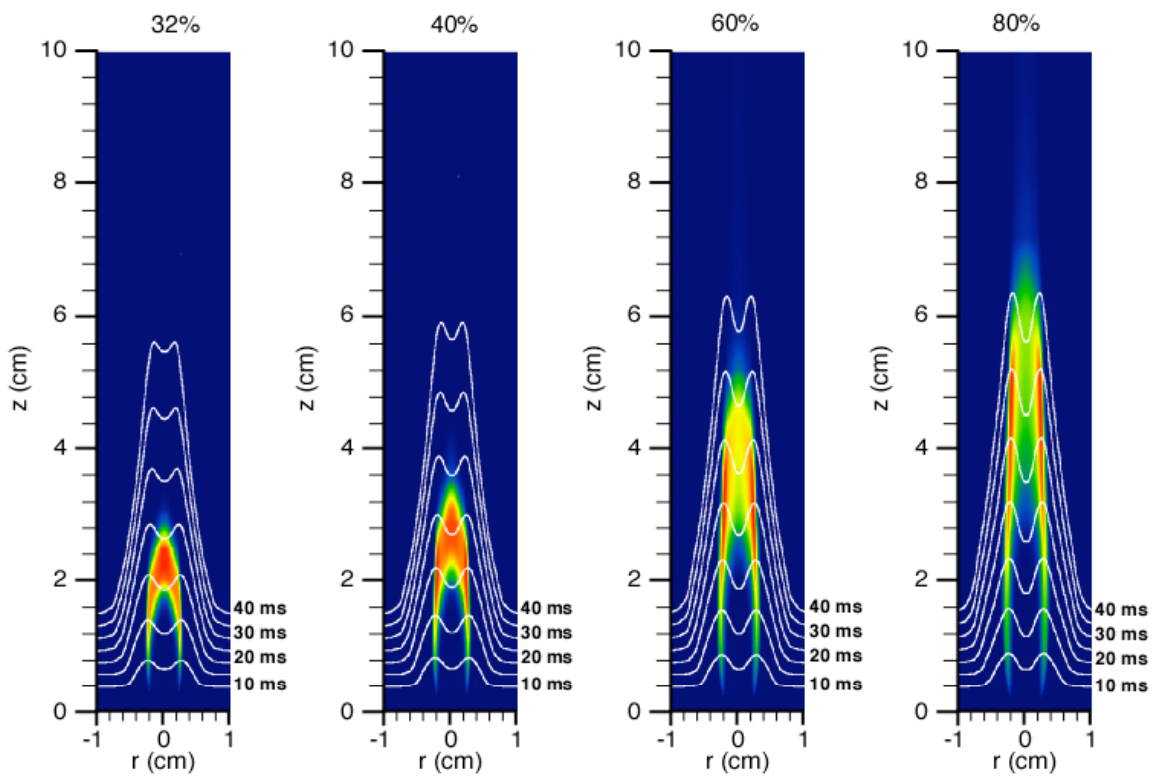


Figure 13. Contours of soot volume fractions along with isopleths of residence times.

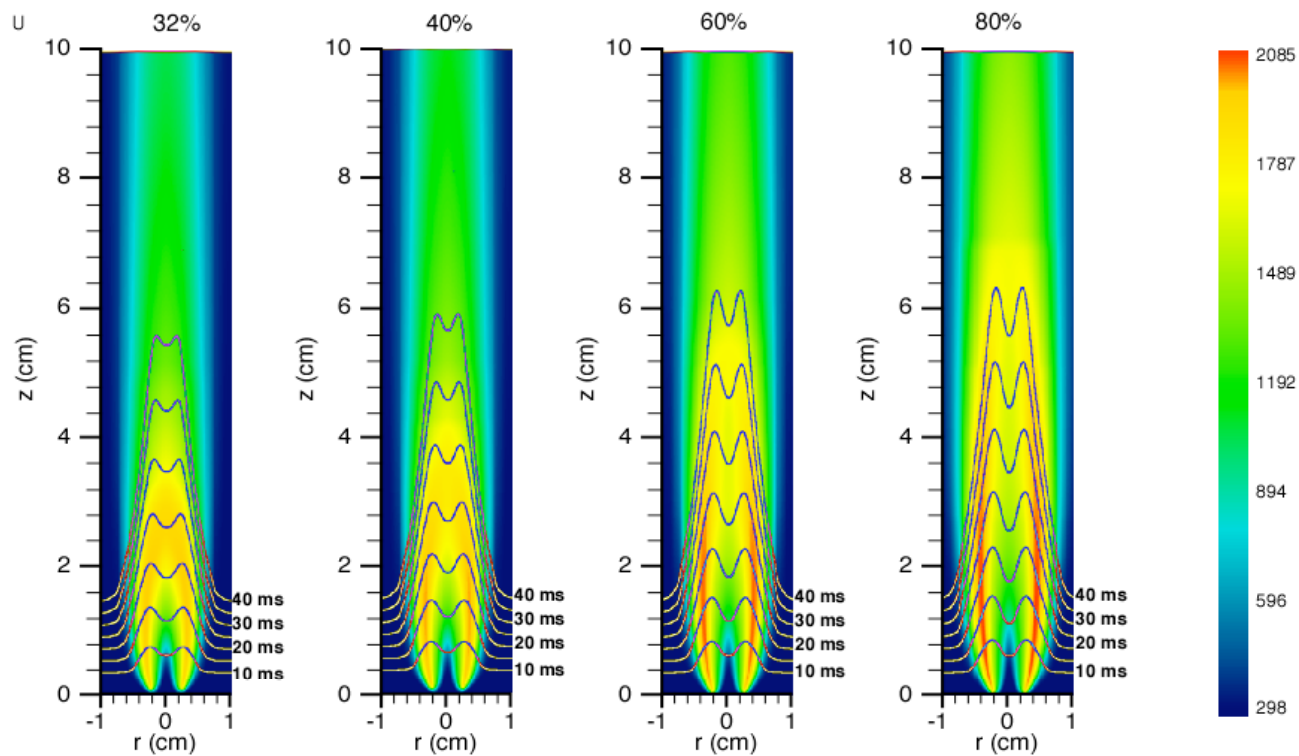


Figure 14. Temperature isotherms with isopleths of residence times. Note the adjustment of the color scale to illustrate the higher wing temperatures as the fuel fraction increases.

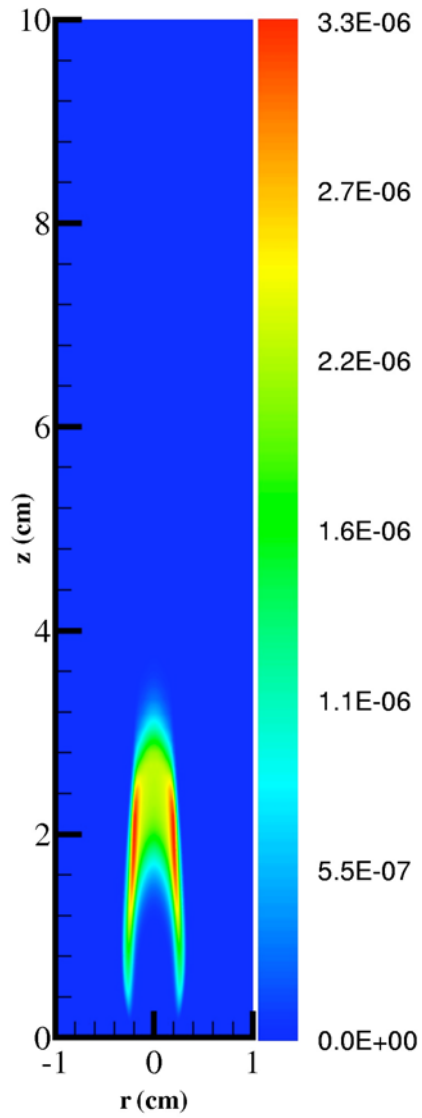


Figure 15. Computational soot volume fraction for the lower velocity 80% flame.

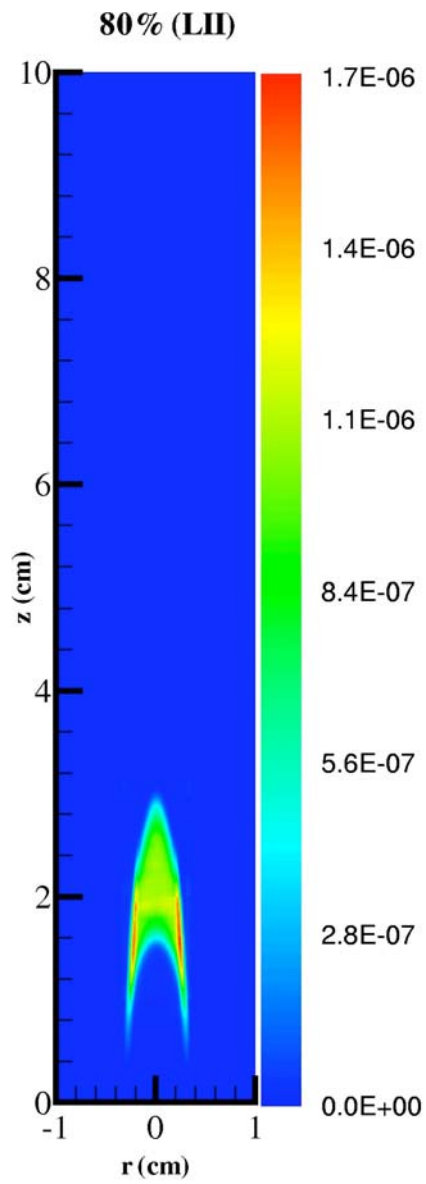


Figure 16. Experimental (LII) soot volume fraction for the lower velocity 80% flame.

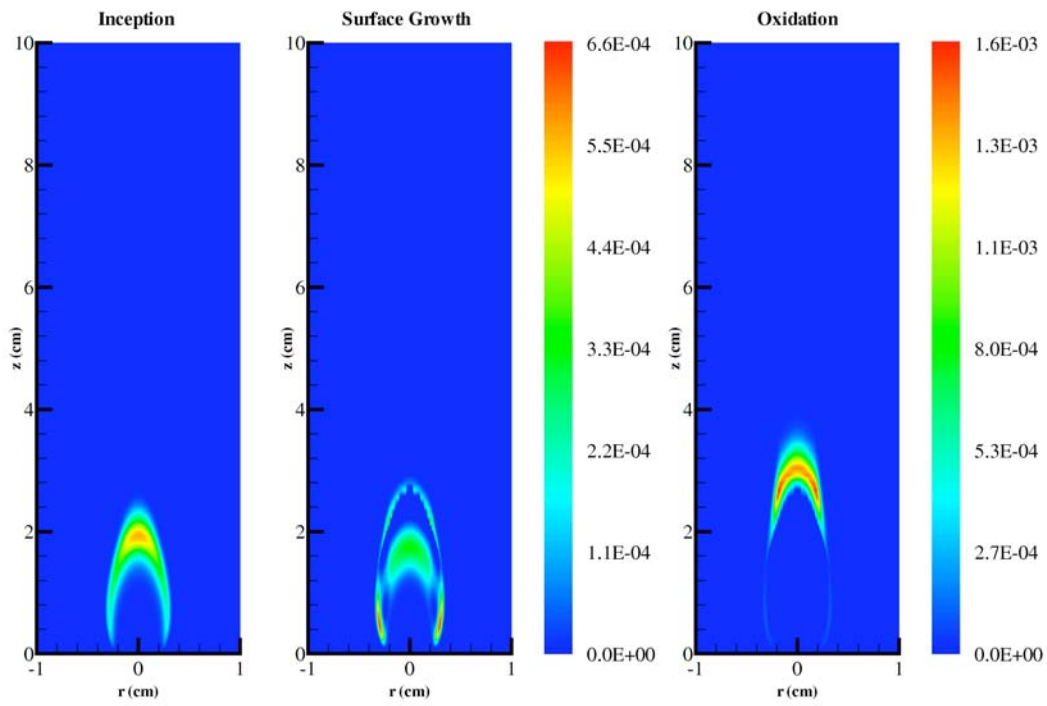


Figure 17. Computed contours of inception, surface growth and (-) oxidation rates (gm/cc/sec) for the lower velocity 80% flame.